



HAL
open science

Surrogate model development for optimized blended-wing-body aerodynamics

Hema Aubeelack, Stéphane Segonds, Christian Bes, Thierry Druot, Joël
Brezillon, Adrien Bérard, Marylène Duffau, Guillaume Gallant

► **To cite this version:**

Hema Aubeelack, Stéphane Segonds, Christian Bes, Thierry Druot, Joël Brezillon, et al.. Surrogate model development for optimized blended-wing-body aerodynamics. *Journal of Aircraft*, 2022. hal-03827321

HAL Id: hal-03827321

<https://hal.science/hal-03827321>

Submitted on 24 Oct 2022

HAL is a multi-disciplinary open access archive for the deposit and dissemination of scientific research documents, whether they are published or not. The documents may come from teaching and research institutions in France or abroad, or from public or private research centers.

L'archive ouverte pluridisciplinaire **HAL**, est destinée au dépôt et à la diffusion de documents scientifiques de niveau recherche, publiés ou non, émanant des établissements d'enseignement et de recherche français ou étrangers, des laboratoires publics ou privés.

Surrogate model development for optimized blended-wing-body aerodynamics

Hema Aubeelack*

*Airbus Operations SAS, 316 route de Bayonne, 31300 Toulouse, France &
ICA UMR CNRS 5312, 3 rue Caroline Aigle, 31400 Toulouse, France*

Stéphane Segonds[†], Christian Bes[‡]

*Université de Toulouse, UPS/INSA/ISAE/Mines Albi, ICA UMR CNRS 5312
3 rue Caroline Aigle, 31400 Toulouse, France*

Thierry Druot[§]

*École nationale de l'aviation civile, 7 avenue Edouard Belin, 31400 Toulouse &
Airbus Operations SAS, 316 route de Bayonne, 31300 Toulouse, France*

Joël Brezillon[¶], Adrien Bérard^{||}, Marylène Duffau^{**} and Guillaume Gallant^{††}
Airbus Operations SAS, 316 route de Bayonne, 31300 Toulouse, France

In the conceptual design phase of conventional-configuration aircraft, calibrated low-fidelity methods provide sufficiently accurate estimates of aerodynamic coefficients. It has been observed, however, that for blended-wing-body aircraft, important flow effects are not captured adequately with low-fidelity aerodynamic tools. Consequently, high-fidelity methods become necessary to study blended-wing-body aerodynamics. Since repeated function calls are needed in an optimization loop, high-fidelity analysis is prohibitively expensive in the conceptual design phase, where several optimization scenarios are considered. In this paper, the integration of high-fidelity data for blended-wing-body aircraft for a mission calculation module is presented. A surrogate model based on Gaussian processes (GPs) with acceptably low prediction error is sought as an alternative to RANS CFD. Three adaptations are considered: sparse GPs, mixtures of GP approximators, and need-based filtering for GP. The results provide benchmark values for this case and show that the combination of subsonic and transonic behaviors in the training set is problematic and that, for the considered datasets, sparse GP models suffer from oversmoothing while mixtures of GPs models suffer from overfitting. From the error levels, it is observed that a GP with an infinitely-differentiable squared exponential kernel based on

*PhD Student, Future Projects Department, hema.aubeelack@airbus.com

[†] Assistant Professor, stephane.segonds@univ-tlse3.fr

[‡] Professor, christian.bes@univ-tlse3.fr

[§] Associate Professor, thierry.druot-ext@enac.fr

[¶] Aerodynamics M&T Engineer, Flight Physics Department, joel.brezillon@airbus.com

^{||} Technology Project Management, Flight Lab, adrien.berard@airbus.com

^{**} Senior Engineer, Future Projects Department, marylene.duffau@airbus.com

^{††} Senior Engineer, Future Projects Department, guillaume.gallant@airbus.com

reduced data pertinent to mission analysis is the most effective option.

I. Introduction

AVIATION is a sector with important fuel consumption levels and greenhouse gas emissions, with a 2% share of the global human-induced CO₂ emissions in 2019 [1]. As economical and ecological goals go hand in hand with a direct link between aircraft efficiency and fuel costs for operations, a transition geared towards aircraft emissions reduction has been a top priority for aircraft manufacturers and airlines alike over the last decade. In 2009, the International Air Transport Association (IATA) set three key targets for 2050, one of which is a 50% reduction in net aviation CO₂ emissions relative to 2005 levels [2]. To this end, aviation experts have relentlessly been exploring the development of new technologies or the improvement of existing ones to reduce emissions linked to air transport. For instance, specific areas that have received more attention in recent years are the decarbonization of the aviation industry by using alternative energy sources [3–5], unconventional aircraft configurations [6], and improved propulsion-airframe integration [7, 8] with higher-performance or new-configuration engines such as open rotors [9] and boundary-layer-ingesting engines [10] analyzed with exergy-based performance approaches [11].

A firm interest in the blended-wing-body (BWB), an unconventional aircraft configuration, continues to exist because it presents an opportunity for significant fuel burn reduction compared to conventional aircraft [12] owing to its minimal wetted area. As a commercial aircraft for passenger transport, the BWB configuration is the most promising new concept to address the ever-increasing demand, with an estimated 40–60% increase in passenger numbers for a limited increase in aircraft movements [13]. There are large and recently active BWB projects from the two major aircraft manufacturers who dominate the market. On Boeing’s side, the X-48C [14] was an experimental unmanned aerial vehicle used to conduct several flight tests in collaboration with NASA until April 2013, and is a precursor to their next planned larger demonstrator. More recently, Airbus revealed its BWB demonstrator, the Model Aircraft for Validation and Experimentation of Robust Innovative Controls (or MAVERIC), at the Singapore Air Show in February 2020 [15].

In recent years, advances in algorithms, computational tools, and computing capabilities have changed the way in which aircraft design is performed. As a result, several new ways of modeling and optimizing aircraft configurations have emerged, particularly for BWB aircraft, where the design problem is highly multidisciplinary in nature. To solve such a complex optimization problem, the problem needs to be constructed to keep the number of variables and computing time reasonable relative to the computing capabilities. To address the nature and large number of variables (273 in this problem) with tight couplings among aerodynamic performance, trim, and stability, a series of tractable aerodynamic optimization studies was presented, where aerodynamic shape optimization studies minimized the drag coefficient under lift, trim, static margin, and center plane bending moments constraints [16]. Another main challenge of BWB design, control architecture sizing, was tackled using

a new coupled approach [17]. Improved decision-making techniques in early multidisciplinary design allowing designers to combine mathematical model predictions with their confidence level in the underlying information have been applied to the BWB [18]. Detailed studies using advanced aerodynamic tools have allowed trade-offs between aerodynamic efficiency and wing structure weight at transonic speed to be made [19].

Over the last half-decade, more advanced mathematical models for aerodynamics including surrogate models have proved to be efficient in surrogate-based design optimization for several applications, such as vortex generators for a tiltrotor geometry [20], a wing fence for unmanned aerial vehicles including parametric studies [21], and the aerodynamic shape optimization of a natural-laminar-flow wing [22]. Multiobjective aerodynamic optimization using variable-fidelity models and response surface surrogates has been applied to airfoil design to allow high-fidelity optimization at low computational cost using a reduced number of high-fidelity simulations [23]. Gradient-based optimization using a surrogate model was applied to a massively multipoint aerodynamic shape design for a conventional aircraft to leverage both efficient gradient-based optimization and speedy evaluations of surrogate models [24]. A surrogate modeling technique was proposed with dimensionality reduction specifically to tackle distributed fluid systems by modeling subdomains with matching interface conditions [25]. Aerodynamic surrogate modeling has also been extended to treat uncertainty aspects for the case of Gaussian surrogate dimension reduction for efficient reliability-based design optimization [26], and for the surrogate-based robust optimization of low-noise open rotors using dual-level Kriging [27].

A challenging topic in BWB aircraft conceptual design is aerodynamic performance estimation, which is of particular interest early on owing to the direct dependence of block fuel on aircraft drag. In aerodynamics, low-fidelity tools often relying on 2D analysis are generally used in the conceptual design phase owing to the fast solution time of the order of seconds at most on a personal computer, whereas high-fidelity tools, with which computations often require high performance computing (HPC) clusters, tend to be better adapted to the preliminary design phase, which is a subsequent, more detailed design phase. However, in the case of BWB aircraft, limitations were reported in establishing a tangible link between 2D flows around airfoils and 3D flows [28], highlighting the inadequacies of 2D-based low-fidelity methods for this unconventional aircraft. A separate study concluded that standard drag build-up methods based on flat plate aerodynamics, which low-fidelity tools on, do not hold owing to the thick airfoils and large chord lengths of the BWB centerbody [29]. Wind tunnel tests on a BWB model showed that, in addition to the expected potential flow lift mechanism, a vortex flow mechanism is present [30] which is not accounted for in traditional low-fidelity models.

In view of the complexity of BWB aerodynamics, a different approach is proposed based on high-fidelity computations. This is required because a very specific problem exists in conceptual overall aircraft design (OAD) when it comes to BWB aerodynamics: the usual low-fidelity methods fail, while high-fidelity methods are computationally prohibitively expensive to be integrated in a multidisciplinary framework. **While many approaches have been proposed in the literature, the use of surrogate modeling for aerodynamic data after high-fidelity optimization has not been**

dealt with previously. The objective of the work presented in this paper is to demonstrate how high-fidelity CFD data can be used to build a model to relate the Airbus BWB planform shape to its corresponding optimized aerodynamic performance within the design bounds. In the conceptual OAD phase, the capability of target-setting is the intended goal: realistic and achievable targets for an aircraft design need to be determined despite the limited detailed knowledge on the aircraft. In other words, in the design loop, the aircraft designer needs the ability to estimate the final performance that an aircraft configuration will have by the end of detailed design phase knowing only the main parameters of that configuration. Target-setting is normally achieved using low-fidelity tools and experience with similar prior operational aircraft, which are lacking in the case of unconventional arrangements like the BWB. As a proposed solution, a database of computational fluid dynamics (CFD) optimization results is used as basis to develop a surrogate model to act as an inexpensive aerodynamic calculation method quick enough to be used directly in a multidisciplinary OAD framework.

In Section II of this paper, the BWB design philosophy is explained to support the description of the database generation process in Section III. In Section IV, the approach to generating and evaluating potential surrogate models is presented to highlight the important criteria in model selection. Finally, in Section V, results specific to the BWB aerodynamic database used in this study are shown to illustrate how a well-chosen and well-tuned surrogate model can perform to enable the use of aerodynamic data for wide-scope applications beyond strictly aerodynamic studies.

II. Design Philosophy

The attempt to model BWB aerodynamics in this paper is to provide information on one of many aspects in a multidisciplinary design study. However, an aspect of aerodynamic design taken into consideration in this study but not in the published literature is the consistency in maturity level across analyses. Specifically, to ensure that the aerodynamic maturity level is universal, a design philosophy is adopted whereby, for any multidisciplinary analysis, aerodynamic cruise-optimal performance can be sensibly assumed. This is important because failure to achieve consistent levels of maturity in the same discipline leads to flawed comparisons and incorrect design decisions. In the BWB case, this is even more important than in the case of conventional aircraft because the thick centerbody airfoils make the BWB more easily susceptible to shock wave formation. This means that a BWB with well-chosen thickness distributions will always outperform one with poorly-chosen thickness distributions, even if the reverse could be true once they are both aerodynamically optimized.

For the OAD problem, a design philosophy has been adopted wherein different sets of parametrization are used, with one top-level set of variables common to all the disciplines involved. Six top-level variables were chosen to uniquely define the planform shape to allow changes in chord lengths and section spans, causing variations on a global level. In Figure 1, dimensions for the centerbody, which comprises sections 0–3, are the centerbody sweep angle (ϕ_c) and the centerbody chord length (L_c). Smoothness of transition between section 3 of the centerbody and section 4 of the outer wing is controlled using a kink parameter (x_{out}), which allows movement of the leading edge of section 4 in the

x -direction. The outer wing chord (c_{out}), outer wing span (b_{out}), and outer wing quarter-chord sweep angle (ϕ_{out}) are the parameters that complete the definition of the BWB planform. The chord lengths for sections 1–3 scale linearly with L_c , and those for sections 4–7 with c_{out} . The design vector \mathbf{x}_p is made up of the top-level variables, such that $\mathbf{x}_p = [\phi_c, L_c, x_{out}, c_{out}, b_{out}, \phi_{out}]$.

For CFD computations to be possible on the BWB, a three-dimensional shape is defined from the two-dimensional planform corresponding to the design vector \mathbf{x}_p . To permit this, a lower level set of variables for aerodynamic parametrization is used to describe the sectional shape of the BWB along the span of the aircraft. Airfoil design is a field of study in itself, and several parametrization techniques exist in the literature [31]. Here, the airfoils are parametrized to allow changes in the local incidence (or twist), camber and thickness distributions to produce relatively local variations in the transverse plane. In the aerodynamic parametrization employed, 66 shape variables making up the aerodynamic design vector \mathbf{s} are used to describe the airfoils of the BWB using non-uniform rational B-splines, more commonly known as NURBS [32]. In this BWB application, there is a particular volumetric constraint which is worth mentioning owing to the consideration of space allocation requirements for the aircraft interior within the centerbody, as shown in Figure 2.

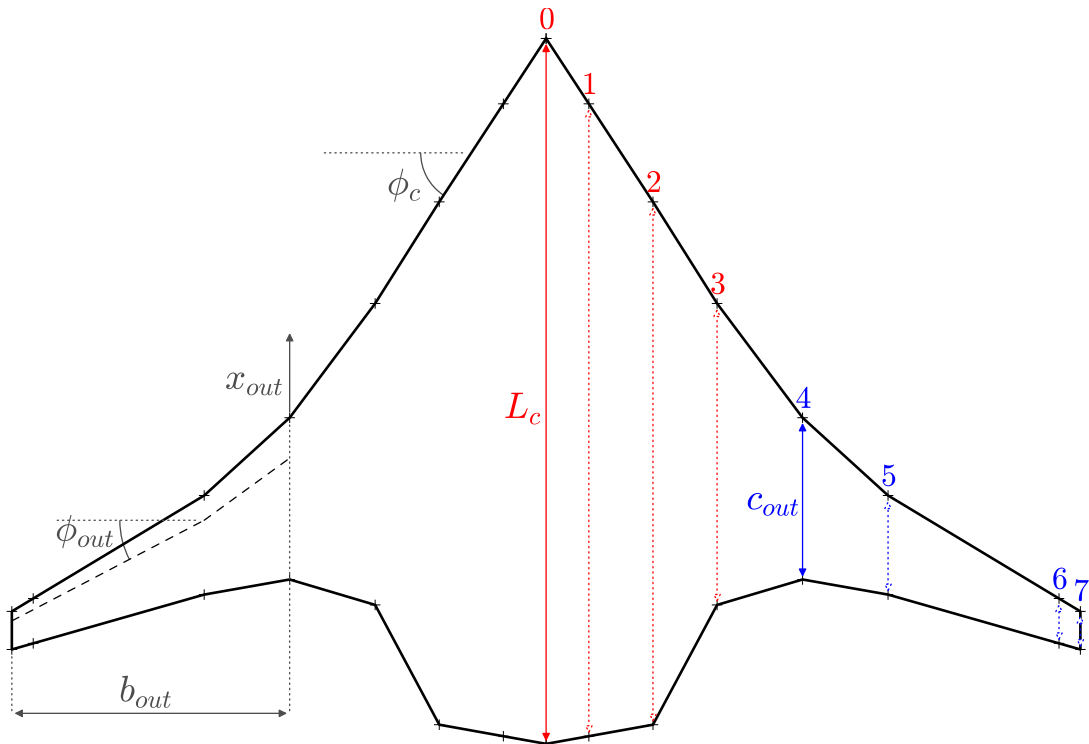


Fig. 1 Planform parametrization. Six top-level variables drive the BWB planform shape.



Fig. 2 Section constraints at the centerbody driven by internal volume requirements.

III. Aerodynamic Database Generation

Careful thought must be given to designing the structure of a database of aerodynamic optimization data for surrogate model construction. If the 66 airfoil and 6 planform variables are considered at once in the multidisciplinary analysis chain, the required size of the DoE quickly becomes intractable with all 72 design variables. A way of improving tractability and meaningfulness is to develop a database containing aerodynamic data obtained through single-point optimization at the airfoil level for several BWB planform shapes, thereby creating a solution space where, for each planform shape \mathbf{x}_p , optimal airfoil variables $\mathbf{s}^*(\mathbf{x}_p)$ at the optimal angle of attack $\alpha^*(\mathbf{x}_p)$ can be assumed for the dominating flight condition, cruise. Further assuming continuity in this aerodynamic cruise-optimal design space, the aircraft designer can interpolate to estimate the performance of any planform shape \mathbf{x}_p without knowledge of $\mathbf{s}^*(\mathbf{x}_p)$ and $\alpha^*(\mathbf{x}_p)$, resulting in an independence from the computationally-intensive optimization process required to compute $\mathbf{s}^*(\mathbf{x}_p)$ and $\alpha^*(\mathbf{x}_p)$. It is useful to note that the simultaneous consideration of all 72 shape variables in a DoE would impede on the freedom to perform optimization. In effect, the aerodynamic optimization conducted for each BWB planform shape is a means of reducing the dimensionality of the design space to a cruise-optimal design space, thus enabling the discard of non-interesting solutions. A very similar approach has been used by the same research team to create a cruise-optimal database to demonstrate a robust optimization methodology [33].

A. Aerodynamic optimization process

For any fixed planform \mathbf{x}_p , an aerodynamic optimization can be conducted with the pressure drag coefficient ($C_{D,p}$) as objective function. The flow field is computed using *elsA*, a CFD solver developed by ONERA [34]. The lift force is the component normal to the direction of far-field flow, while the drag force is the component opposing the direction of the far-field flow. Force coefficients are obtained by normalizing the forces using the dynamic pressure and a fixed reference area corresponding to that of a reference BWB aircraft geometry.

In the computations, the discretized Navier-Stokes equations are used in conjunction with the Spalart–Allmaras [35] turbulence model to simulate the flow field around the three-dimensional BWB aircraft. A discrete adjoint method is used to compute sensitivities for the gradient descent. In the optimization problem solved, a Limited-memory Broyden-Fletcher-Goldfarb-Shanno (LBFGS) optimization algorithm is used to find the minimum $C_{D,p}$ at target lift ($C_{L,\text{target}}$):

$$\begin{aligned}
& \underset{\mathbf{s}, \alpha}{\text{minimize}} && C_{D,p}(\mathbf{s}, \alpha) \\
& \text{subject to} && C_L(\mathbf{s}, \alpha) = C_{L,\text{target}}
\end{aligned} \tag{1}$$

where α is the angle of attack, and where forces on the BWB are calculated using integration methods for the pressure field acting on the aircraft surface assuming negligible viscous shear stresses [36]. The target lift constraint is treated implicitly by adjusting α automatically during the CFD run, and the optimization problem is treated as an unconstrained problem. The other drag component owing to surface friction of the air, friction drag ($C_{D,f}$), is neglected. It was experimentally verified, using additional simulations, that this simplification does not impact the optimization solution because the wetted area variations due to airfoil shape changes are not significant at fixed \mathbf{x}_p . A constraint corresponding to a constant lift coefficient for steady, level flight for all planforms at the cruise condition is enforced specifically to ensure minimum drag at the target lift coefficient. Optimization problem 1 is a single-point aerodynamic optimization conducted at the cruise condition, such that the sectional shape given by $\mathbf{s}^*(\mathbf{x}_p)$ for a planform \mathbf{x}_p can thus be described as being cruise-optimal.

B. Design of experiments

The resolution of optimization problem 1 being computationally expensive, a DoE approach with a fixed budget is chosen to construct a database for cruise-optimal BWB aerodynamics. A Latin hypercube sampling technique is used to generate a stratified near-random 50-point set of planform shapes in a six-dimensional unit hypercube covering the entire design space, wherein the top-level parameters are normalized between 0 and 1. The 50 optimization runs, each corresponding to a planform shape \mathbf{x}_p in the DoE, are conducted at target C_L , with 48 of these runs being convergent on an optimal solution. As a result, $(\mathbf{s}^*(\mathbf{x}_p), \alpha^*(\mathbf{x}_p))$ for $\mathbf{x}_p^{(i)}$, $i = 1, \dots, 48$ are obtained, defining the optimal sectional shapes and angle of attack of the BWB for cruise.

C. Polar generation

For each optimized BWB defined by $(\mathbf{x}_p, \mathbf{s}^*(\mathbf{x}_p))$, the aerodynamic performance over an array of flight conditions is required to evaluate its overall performance in the OAD chain. To this end, the flow field for each aerodynamic cruise-optimal planform shape $(\mathbf{x}_p^{(i)}, \mathbf{s}^{*(i)}(\mathbf{x}_p))$, $i = 1, \dots, 48$, is computed at six Mach numbers and ten angles of attack to construct a set of drag polars, which consist of pairs of total drag coefficient (C_D) and lift coefficient values calculated using a far-field approach [37]. The resulting database contains 2880 points characterizing the aerodynamic performance of 48 BWB planforms, first optimized at the cruise condition to determine $\mathbf{s}^*(\mathbf{x}_p)$, then computed for 60 flow conditions. Of the 2880 computations, 21 CFD simulations did not converge to the required tolerances owing to the difficulty of convergence at the highest angle of attack and highest Mach number caused by phenomena such as flow separation in the onset of stall and shock wave formation, resulting in a database size of 2869 points.

D. Summary of database generation process

Figure 3 provides a schematic view of the process to construct the database used in the next section. For each planform shape \mathbf{x}_p in a set of planform shapes, the DoE X in this case, the aerodynamic cruise-optimal sectional variables $(\mathbf{s}^*(\mathbf{x}_p), \alpha^*(\mathbf{x}_p))$ are determined using gradient-based aerodynamic shape optimization with CFD. The drag polar for each cruise-optimal planform shape $(\mathbf{x}_p, \mathbf{s}^*(\mathbf{x}_p))$ is then constructed by computing the force coefficients for 60 (M, α) combinations to construct the final database. Of the 3000 expected points in the database, 131 are unavailable owing to the non-convergence of the aerodynamic shape optimizer or of the CFD computation.

E. Properties of the aerodynamic database

Before constructing an approximation model, it is worthwhile to inspect the structure of the underlying data. In Figure 4, the cumulative distribution function (CDF) of the DoE variables, which are the variables in \mathbf{x}_p , show near-uniformity in agreement with the LHS sampling scheme used, with two apparent gaps corresponding to the two planform shapes for which the CFD optimization did not converge. Note that every point in Figure 4 stands for 60 CFD computations for the different flight conditions, or fewer in cases where the computation did not converge. The distributions for M and α are not plotted because they consist of a few evenly-distributed discrete values. From Figure 4, the Latin hypercube structure with two simulations amiss is apparent, and it is demonstrated that the design space can be considered as being uniformly represented over the six BWB planform variables.

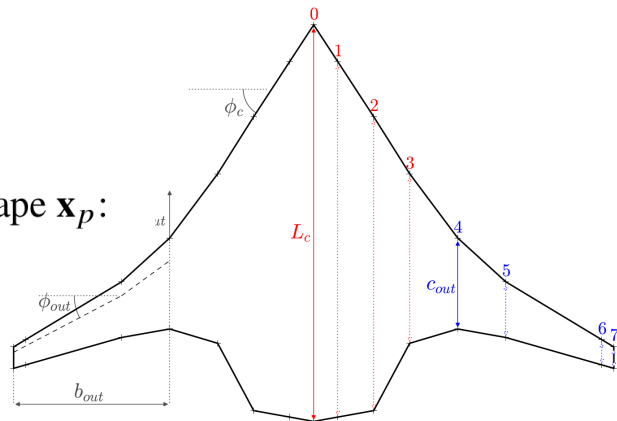
Similarly, the cumulative distributions of the force coefficients are plotted in Figure 5. The C_L cumulative distribution roughly resembles a normal one, with two waves appearing for $C_L \leq 0.05$. This can be explained by the fact that the C_L distribution consists of 10 nearly normal distributions, each corresponding to a particular α . For the first two values of α , values for C_L have smaller ranges and do not overlap with neighboring distributions as much as other α , decreasing the homogeneity in the superposition of the 10 individual distributions. As for C_D , the cumulative distribution takes the shape of a truncated normal distribution, reflecting that C_D is in fact reduced by the CFD optimization process to as little as the physics can allow, with the truncated part of the normal distribution being physically infeasible. In the surrogate model, C_L is an independent variable; its distribution, while not approximately uniform as would be ideal, continuously covers the C_L range. The C_D values are well distributed over their range, although this distribution is not a full Gaussian distribution, as would be preferred for the dependent variable.

F. DoE enrichment

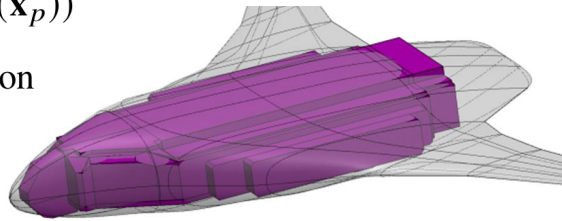
In a problem treated separately, DoE enrichment is performed, where points are added to the initial DoE to increase model accuracy by improving knowledge in the most uncertain regions of the design space. These additional points serve as an extra set of data to evaluate model prediction quality on data not known to the model beforehand, and to enrich the initial LHS DoE for the construction of a final model.

PERFORM FOR EACH PLANFORM IN THE DESIGN OF EXPERIMENTS

1) For the planform shape \mathbf{x}_p :



2) Calculate $(\mathbf{s}^*(\mathbf{x}_p), \alpha^*(\mathbf{x}_p))$
using CFD optimization



3) Calculate force coefficients
for 60 (M, α) flow conditions
for the geometry $(\mathbf{x}_p, \mathbf{s}^*)$

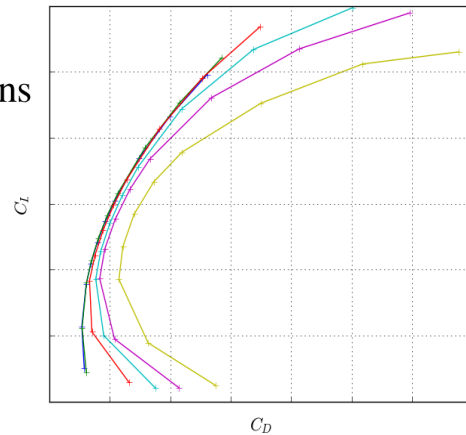


Fig. 3 Aerodynamic database generation process to find cruise-optimal sectional shapes and the corresponding drag polars for all planforms considered.

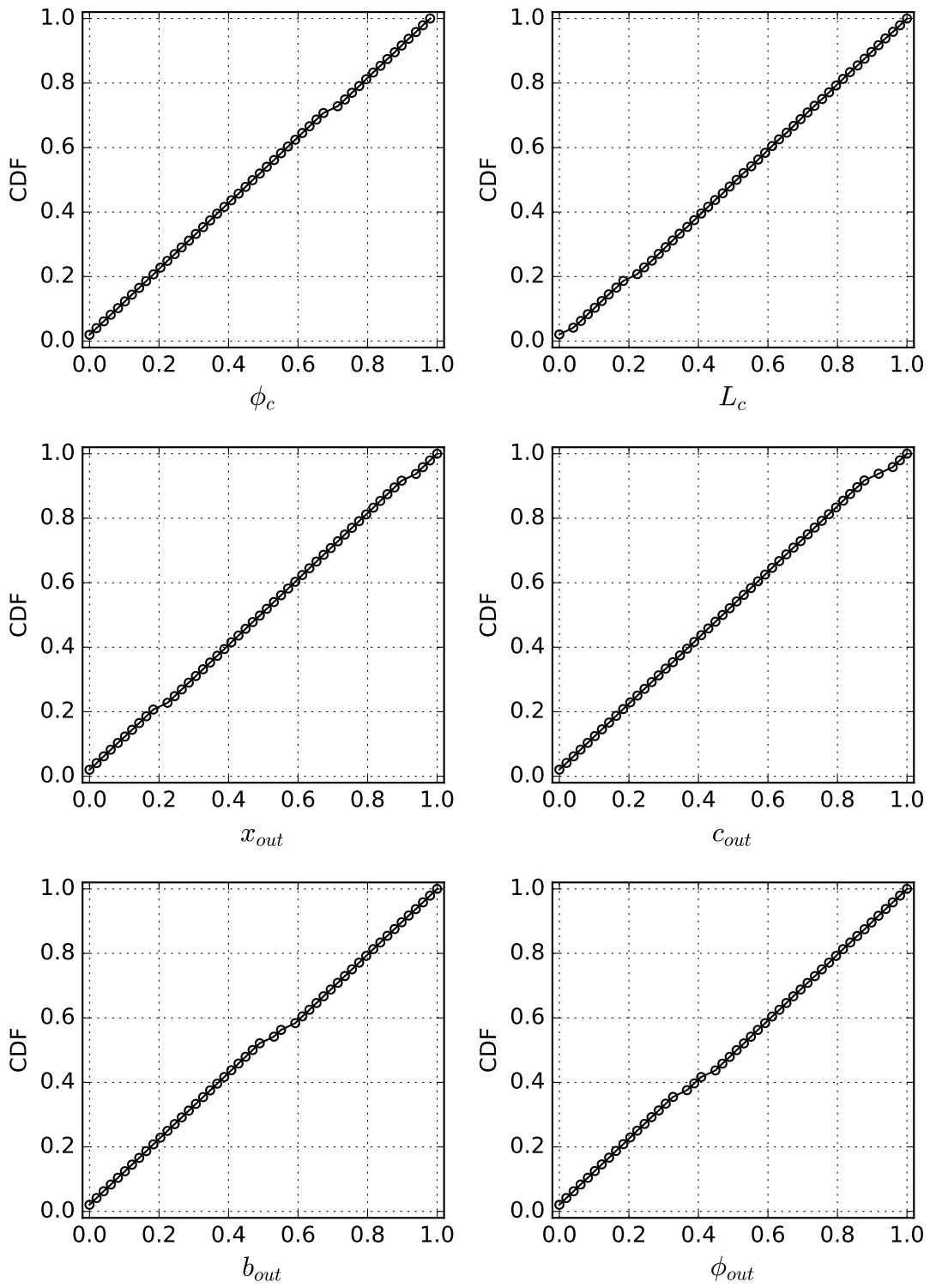


Fig. 4 CDF of DoE variables in aerodynamic database.

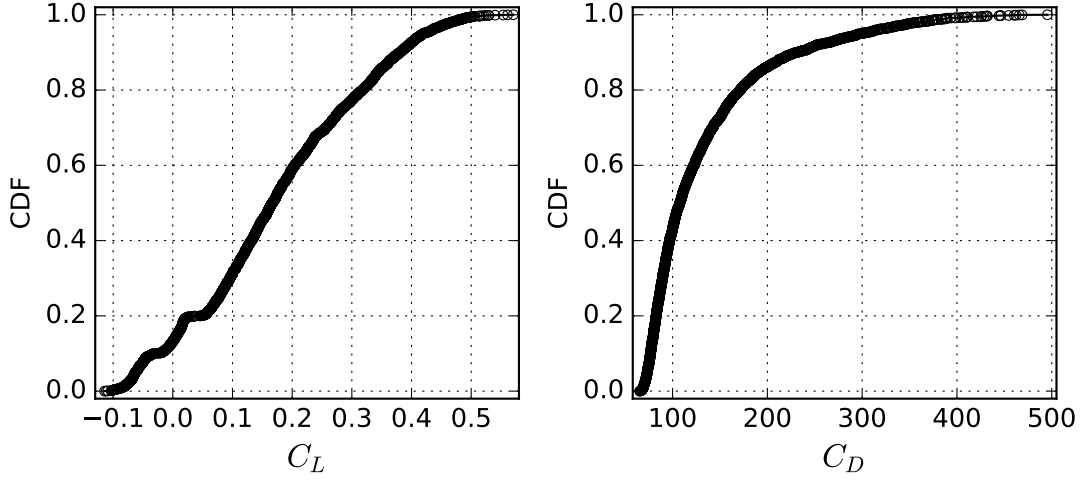


Fig. 5 CDF of force coefficients in the aerodynamic database.

The uniform criterion, which seeks the points with the largest Euclidean distance from the other points, and the maximum variance criterion, which seeks the points with the highest uncertainty, have a strong tendency to choose corners of the design hypercube. In contrast, the integrated mean-square-error gain–maximum variance criterion, selected to enrich the DoE, identifies the points which most benefit the model by reducing the integrated mean-square-error over the design space \mathbb{X} while considering the regions with the highest variance:

$$I = \frac{\hat{\sigma}^2(\mathbf{x}|X)}{|\mathbb{X}|} \int_{\mathbb{X}} (\hat{\sigma}(\mathbf{u}|X) - \hat{\sigma}^2(\mathbf{u}|X \cup \mathbf{x})) d\mathbf{u} \quad (2)$$

In total, the drag polars for 13 additional planform shapes are available. These constitute the verification dataset.

IV. Surrogate Modeling Approach for OAD

In terms of computational cost, the aerodynamic optimization process for one planform shape requires on average a wall-clock time of 175 hours using 32 processors of an HPC5 supercomputer. It is clear that such an expensive tool cannot viably be integrated into a multidisciplinary OAD framework which needs to execute a complete run in a few minutes at the most on a personal computer. In this section, the modeling techniques appropriate for this type of problem and database size are described.

A. Objective and formulation

The objective in building a surrogate model which runs in seconds on a personal computer is to replace the resource-intensive HPC-based process of aerodynamic optimization to identify the optimal $\mathbf{s}^*(\mathbf{x}_p)$ for any \mathbf{x}_p followed by computations for different flight conditions using CFD, for each \mathbf{x}_p . The model sought is of the form

$$C_D = \hat{f}(\mathbf{x}_p, M, C_L) \quad (3)$$

to match the format required for use in the OAD mission calculation process, where C_L is a function of \mathbf{x}_p, M, α , and $\mathbf{s}^*(\mathbf{x}_p)$ is assumed. It is desirable to have C_D as a function of C_L rather than of α because C_L can be used directly to calculate the force needed to balance the aircraft weight or to execute the planned mission.

B. Approximation using Gaussian processes

Let the underlying data for constructing a surrogate model be the DoE with sampling plan $X = \{\mathbf{x}^{(1)}, \mathbf{x}^{(2)}, \dots, \mathbf{x}^{(N)}\}^T$, $\mathbf{x} \in \mathbb{R}^k$ consisting of N computations with responses $\mathbf{Y} = \{y^{(1)}, y^{(2)}, \dots, y^{(N)}\}^T$. There are several ways in which to construct the approximation function \hat{f} , as will be described in the next subsection. In this application, the construction of \hat{f} is to be constructed using the *GTApprox* tool in the *Datadvance pSeven* (ex *MACROS*) algorithmic library [38]. For the size and structure of the input database, the approximation methods available are based on Gaussian processes, described hereafter.

Let

$$f(\mathbf{x}) \sim \mathcal{G}(m(\mathbf{x}), k(\mathbf{x}, \mathbf{x}')) \quad (4)$$

where \mathcal{G} denotes the prior of a GP on f with mean function $m(\mathbf{x})$ and covariance function $k(\mathbf{x}, \mathbf{x}')$. Here, the exact formulation assumes that the data is completely noise-free and inherently forces the model to go through the data points.

The mean and covariance functions are given by

$$\begin{aligned} m(\mathbf{x}) &= \mathbb{E}[f(\mathbf{x})] \\ k(\mathbf{x}, \mathbf{x}') &= \mathbb{E}\left[(f(\mathbf{x}) - m(\mathbf{x}))(f(\mathbf{x}') - m(\mathbf{x}'))^T\right] \end{aligned} \quad (5)$$

where the covariance function provides a measure of similarity between two points \mathbf{x} and \mathbf{x}' [39] in the dataset. The multivariate normal distribution of this GP can then be expressed as

$$\mathbf{f} \sim \mathcal{N}(\boldsymbol{\mu}, \boldsymbol{\Psi}) \quad (6)$$

where $\boldsymbol{\mu}$ is a mean vector which is set to $\mathbf{0}$ in ordinary Kriging, and $\boldsymbol{\Psi}$ is a positive semidefinite matrix of covariance between each pair of points in the set X ,

$$\Psi(X, X) = \begin{bmatrix} k(\mathbf{x}^{(1)}, \mathbf{x}^{(1)}) & k(\mathbf{x}^{(1)}, \mathbf{x}^{(2)}) & \dots & k(\mathbf{x}^{(1)}, \mathbf{x}^{(n)}) \\ k(\mathbf{x}^{(2)}, \mathbf{x}^{(1)}) & k(\mathbf{x}^{(2)}, \mathbf{x}^{(2)}) & \dots & k(\mathbf{x}^{(2)}, \mathbf{x}^{(n)}) \\ \vdots & \vdots & \ddots & \vdots \\ k(\mathbf{x}^{(n)}, \mathbf{x}^{(1)}) & k(\mathbf{x}^{(n)}, \mathbf{x}^{(2)}) & \dots & k(\mathbf{x}^{(n)}, \mathbf{x}^{(n)}) \end{bmatrix} \quad (7)$$

To predict test values \mathbf{f}_* at a set of locations X_* which are unknown to the model, it is reasonable to assume that test values and known values are drawn from the same distribution [40]. Their joint normal distribution can be written as

$$\begin{bmatrix} \mathbf{f} \\ \mathbf{f}_* \end{bmatrix} \sim \mathcal{N} \left(\begin{bmatrix} \mu \\ \mu_* \end{bmatrix}, \begin{bmatrix} \Psi(X, X) & \Psi(X, X_*) \\ \Psi(X_*, X) & \Psi(X_*, X_*) \end{bmatrix} \right) \quad (8)$$

where $\mu_* = \mu = \mathbf{0}$ and $\Psi(X, X_*)$, $\Psi(X_*, X)$ and $\Psi(X_*, X_*)$ are covariance matrices to augment $\Psi(X, X)$ for the predictions in X_* .

The prior probability distribution corresponds to the distribution before any evidence has been introduced into the model. In contrast, the posterior probability distribution is the probability distribution obtained once the knowledge available to train the model has been considered. In functional space, the posterior distribution is the prior distribution restricted to contain only the functions which are in accordance with the given data. The posterior distribution is essential in order to compute \mathbf{f}_* and can be obtained by conditioning the joint Gaussian prior on the observed data,

$$\begin{aligned} \mathbf{f}_* | X_*, X, \mathbf{f} &\sim \mathcal{N}(\Psi(X_*, X)\Psi(X, X)^{-1}\mathbf{f}, \\ &\Psi(X_*, X_*) - \Psi(X_*, X)\Psi(X, X)^{-1}\Psi(X, X_*) \end{aligned} \quad (9)$$

Using the matrix inversion lemma and the Schur complement with the posterior predictive density $p(\mathbf{f}_* | X_*, X, \mathbf{f}) = \mathcal{N}(\mathbf{f}_* | \mu_*, \Sigma_*)$ yields a vector of predicted means

$$\bar{\mathbf{f}}_* = \Psi(X_*, X)\Psi(X, X)^{-1}\mathbf{f} \quad (10)$$

with variances

$$\Sigma_* = \Psi(X_*, X_*) - \Psi(X_*, X)\Psi(X, X)^{-1}\Psi(X, X_*) \quad (11)$$

In stochastic Kriging, the training set is considered as being imperfect. The most common examples in aerospace engineering are numerical results obtained using simulation models and experimental results from laboratory measurements. They are imperfect because they are uncertain insofar as repeated runs for the same inputs will yield different responses [41]. Instead of considering $f(\mathbf{x})$ as being deterministic, let y be its stochastic equivalent subject to a zero-mean uncertainty ε of variance σ_n^2 ,

$$y = f(\mathbf{x}) + \varepsilon, \quad \varepsilon \sim \mathcal{N}(0, \sigma_n^2) \quad (12)$$

The mean function of the stochastic GP is unaffected by this change. However, the covariance is now, using the independent and identically distributed assumption,

$$\text{cov}(\mathbf{x}, \mathbf{x}') = k(\mathbf{x}, \mathbf{x}') + \sigma_n^2 \delta_{\mathbf{x}, \mathbf{x}'} \quad (13)$$

where δ is the Kronecker delta which equals 1 if and only if $\mathbf{x} = \mathbf{x}'$. Interpretatively, only the correlation values of the training points with themselves, each of value 1, which make up the diagonal of the covariance matrix, have the variance of this noise term ε added. This operation converts the covariance matrix $K(X, X)$ into $K(X, X) + \sigma_n^2 I$. The joint normal distribution of the stochastic GP becomes

$$\begin{bmatrix} \mathbf{y} \\ \mathbf{f}_* \end{bmatrix} \sim \mathcal{N} \left(\begin{bmatrix} \mu \\ \mu_* \end{bmatrix}, \begin{bmatrix} \Psi(X, X) + \sigma_n^2 I & \Psi(X, X_*) \\ \Psi(X_*, X) & \Psi(X_*, X_*) \end{bmatrix} \right) \quad (14)$$

and the posterior predictive density $p(\mathbf{f}_* | X_*, X, \mathbf{y}) = \mathcal{N}(\mathbf{f}_* | \mu_*, \Sigma_*)$ yields the predicted means and variances

$$\begin{aligned} \mathbf{f}_* | X_*, X, \mathbf{y} &\sim \mathcal{N}(\bar{\mathbf{f}}_*, \text{cov}(\mathbf{f}_*)) \\ \bar{\mathbf{f}}_* &= \Psi(X_*, X) [\Psi(X, X)^{-1} + \sigma_n I] \mathbf{y} \\ \text{cov}(\mathbf{f}_*) &= \Psi(X_*, X_*) - \Psi(X_*, X) [\Psi(X, X)^{-1} + \sigma_n I]^{-1} \Psi(X, X_*) \end{aligned} \quad (15)$$

C. Large datasets with Gaussian processes

Because GPs involve the inversion of covariance matrices, the computational complexity is $O(n^3)$. Limitations thus exist on the size of covariance matrices that can be reasonably handled by personal computers. Beyond roughly 1000 points, the matrix calculations start to become demanding in terms of memory and processing needs. However, more advanced techniques exist to enable the use of GPs on large datasets. Two such techniques are considered and described next, sparse Gaussian processes (SGP) and mixtures of approximators (MoA). An additional third approach is proposed, wherein a select subset of points is used to construct a conventional GP model. These three approaches have different mathematical constructions and perform differently for a given dataset, which is studied in the next section.

1. Sparse Gaussian processes

In SGP, a subset of the large training set is the basis for constructing the GP model. To avoid the inversion or factorization of the full covariance matrix, a subset of regressors technique called the V-technique [42] is used to select

part of the full covariance matrix while seeking good properties such as stability. The Nyström method [43] is used conjointly to obtain a low-rank approximation of the covariance matrix, allowing predictions to be made for any point in the design space.

2. Mixture of approximators

When a single approximator does not suffice to construct a global surrogate model, a combination of approximators can be used. This can be particularly useful for spatially inhomogeneous functions or data, and to break up large datasets which cannot be handled in one go. In a Gaussian mixture model, the design space is partitioned into connected sub-domains which correspond to regular behaviors, as described in the following reference [44]. Local models are then constructed for the clusters identified. The Bayesian information criterion [45], also known as the Schwarz information criterion, can provide a recommendation on the number of data clusters to partition the data.

3. Need-based filtering for Gaussian processes

A large enough reduction in the training set size is a way of enabling the direct applicability of GP models. The use of a specially tailored subset is proposed as a means of reducing the number of data points in the training set. In the BWB aerodynamic case, a filtering scheme is defined to remove points from the original database for flight conditions which are not relevant to the BWB mission. This restriction of points to only include flight conditions for climb, cruise, and descent is justified in that the surrogate model is to be used to provide aerodynamic information in the mission analysis module.

D. Metamodel quality assessment: model validation, restitution and verification

In evaluating the quality of a metamodel, three testing steps are followed. First, a validation step is conducted to test the prediction ability at locations which are known to the training set but hidden as an exercise. Second, a restitution step assesses how closely the metamodel can reproduce the data used to train it. Third, a verification step tests the model on a separate dataset.

1. Validation step

Validation is an essential step in ensuring that a surrogate model can make reasonable predictions at locations where it is unaware of the observed value. Split-sample or cross-validation [46] are two ways of partitioning the training set in a validation process. In split-sample validation, a fraction of the training set is hidden, a surrogate model is built using the remaining points, and the points initially set aside are predicted using the model. In k -fold cross-validation, the training set is split into k subsets, and surrogate models are built k times using $k - 1$ subsets to test the prediction for the excluded k^{th} subset. In both validation techniques, training set points are hidden from the model and the quality of the prediction is assessed. The choice of cross-validation method is made by compromising on bias and variance levels.

2. Restitution step

In the restitution step, the surrogate model is interrogated to predict the values that were put into the model. This step is valuable in the case where a stochastic or sparse GP is used, or any other type of surrogate model which does not strictly interpolate between known data points, because it shows where the model is relative to the data points.

3. Verification step

Once satisfactory validation results are obtained, an additional verification set of data containing observations at locations different from the training set is used to test the prediction abilities of the surrogate model. This differs from the validation step in that the surrogate model used for the predictions is based on the full training set, which thereby retains its underlying LHS properties over the planform shapes.

E. Model quality metrics

To describe the performance of a model at any given step, measures of error are needed. The error metrics considered are the root-mean-square error (RMSE), and the relative root-mean-square error (RRMS). RMSE provides an interpretation of the average of the error based on quadratic scoring, and penalizes large errors more compared to the mean absolute error metric. It is given by the square root of the sum of the individual squared errors:

$$\text{RMSE} = \sqrt{\frac{1}{n} \sum_{i=1}^n [y^{(i)} - \hat{f}^{(i)}]^2} \quad (16)$$

The RRMS is the RMSE relative to the variance of the set of individual squared errors. It provides a measure of the average error scaled to y by taking into account the variance on the set of prediction errors,

$$\text{RRMS} = \frac{\sqrt{\frac{1}{n} \sum_{i=1}^n [y^{(i)} - \hat{f}^{(i)}]^2}}{\sqrt{\sigma_y}} \quad (17)$$

To visualize the performance of several candidate surrogate models simultaneously, sets of errors are represented using box-and-whiskers diagrams, which can be compared. In this descriptive statistical tool, the box is bounded by the lower and upper quartiles, and the median which lies in between is drawn inside the box. Whiskers are drawn according to Tukey's original definition at 1.5 times the interquartile range above and below the upper and lower quartiles, respectively. Flier points beyond the whiskers are plotted as individual points.

V. Results

In this section, results of the application of the tools presented in Section IV to the database described in Section III are discussed. The starting point using the full aerodynamic database consists of 2869 points in \mathbb{R}^8 . This database size exceeds the recommended cutoff level of approximately 1000 for conventional GP models, prompting the use of SGP

and MoA techniques. As the nature of the data is not fully known in advance, both squared exponential and exponential covariance functions are considered, and are respectively denoted ‘Sq Exp’ and ‘Exp’ in the results. To use an MoA model, a number of clusters, Cl , needs to be prescribed. According to the Bayesian information criterion, $Cl = 5$ is recommended and is used to construct the MoA models.

At speeds below the cruise speed, a selection of relevant data points for the phases of climb and descent is made by keeping the data points for which $0.08 < C_L < 0.33$, as well as the nearest neighbors outside these bounds (where available) to favor interpolation over extrapolation. This range of C_L values has been obtained from mass variation considerations: assuming the maximum takeoff weight, an extended range possibility, different design choices (landing gear configuration, planform shape, and engine integration), as well as an uncertainty margin, are applied to calculate the range of possible masses of the aircraft, which is then converted into the equivalent range of possible C_L values. Using similar reasoning, the relevant range for the cruise condition for mission analysis is $0.17 < C_L < 0.32$. Flight conditions at speeds beyond the cruise speed are excluded as they are deemed irrelevant to the anticipated mission profile. The resulting filtered new training set consists of 1355 data points, compared to the previous 2869 points. It is adequately small to apply conventional GP techniques, despite the noteworthy construction and validation times of the order of a few hours on a personal computer. As before, the squared exponential and exponential covariance functions are considered.

A. Validation results

For the validation step, ten-fold cross-validation is chosen as an estimator of model error because it offers a suitable compromise between bias and variance for the size of the considered datasets without having a prohibitively high computational cost. In Figure 6, the box-and-whiskers plots for the percentage difference between the true and corresponding predicted values for each of the candidate SGP, MoA and GP models are shown. In a box-and-whiskers plot, the lower the box and whiskers, the lower the errors. The MoA models have the highest errors, followed by the SGP models. The cross-validation errors for the GP models using need-based filtered data are the lowest, with very few points exceeding 10%. It is observed that the MoA models perform significantly worse than the SGP and GP models. It is also observed that the squared exponential kernel has a consistently better cross-validation performance than its exponential counterpart.

Table 1 provides the associated values of the error metrics for this cross-validation step. The performance of MoA models is unacceptably poor, while that of the SGP models is also relatively poor, with cross-validation maximum errors of at best 21.5%. It is worth noting that the highest levels of error occur mainly at the highest angles of attack and the highest Mach numbers for all the metamodels considered.

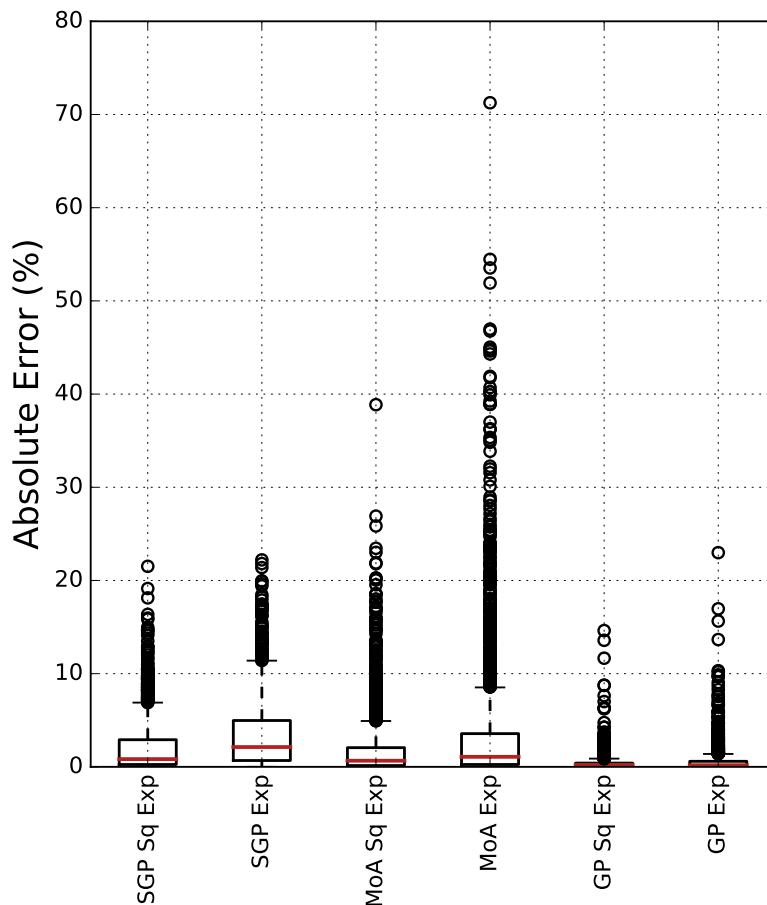


Fig. 6 Ten-fold cross-validation results for full (SGP and MoA) and filtered (GP) database models.

Table 1 Ten-fold cross-validation percent absolute error metrics on the drag coefficient.

| | SGP Sq Exp | SGP Exp | MoA Sq Exp | MoA Exp | GP Sq Exp | GP Exp |
|---------------------------------|---------------|------------|---------------|------------|--------------|-----------|
| Mean (%) | 1.95 | 3.34 | 1.73 | 3.29 | 0.45 | 0.68 |
| Max (%) | 21.52 | 22.21 | 38.86 | 71.26 | 14.62 | 22.99 |
| Median (%) | 0.83 | 2.13 | 0.66 | 1.08 | 0.21 | 0.18 |
| 95 th Percentile (%) | 7.12 | 10.26 | 6.75 | 14.03 | 1.75 | 3.00 |
| 99 th Percentile (%) | 10.52 | 14.91 | 15.03 | 31.69 | 3.60 | 7.56 |
| RMSE or RRMS (%) | 3.18 | 4.81 | 3.38 | 6.87 | 1.08 | 1.69 |

B. Restitution results

Box-and-whiskers plots for the restitution step are shown in Figure 7 with the corresponding error metrics in Table 2. The SGP and MoA models largely fail to pass through the supplied data, as can be seen from the extensive whiskers with high levels of error. Their significant RRMS values demonstrate that these models consistently fail to reproduce the input dataset. The poor performance of the SGP models is attributable to the way in which the importance of points

is weighed, where corners are favored, which results in oversmoothing. Upon inspection of restituted drag polars, it is observed that predicted drag polars from the MoA models do not have the expected quadratic shape owing to the use of combined local models which results in overfitting, thus failing to preserve the characteristic quadratic shape of a drag polar. As in the validation step, the highest levels of error occur predominantly at the highest angles of attack and the highest Mach numbers.

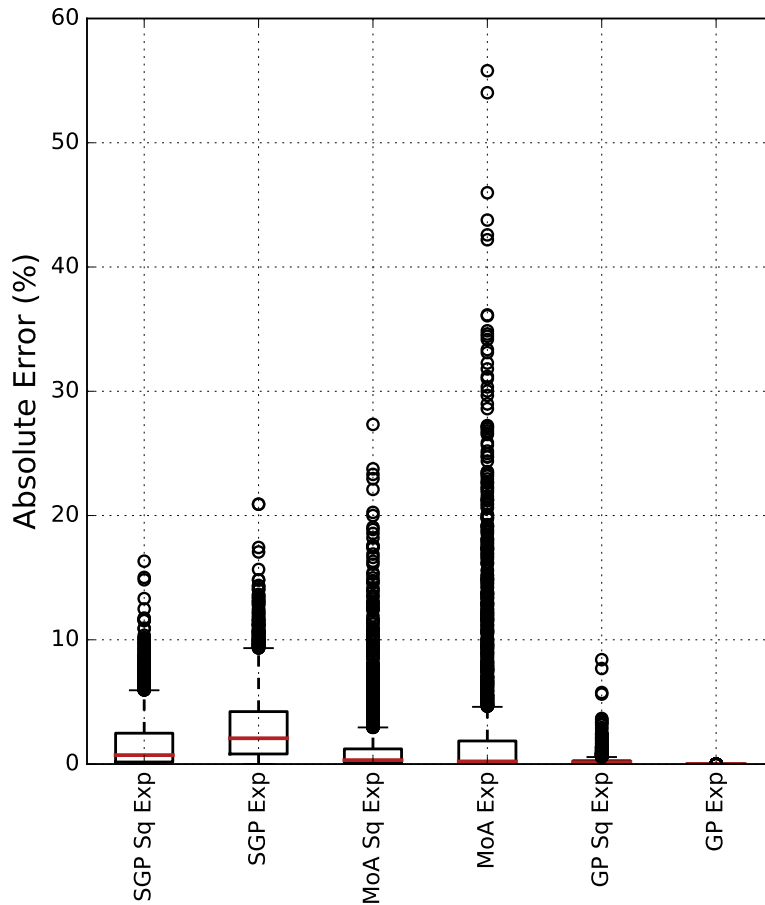


Fig. 7 Restitution results for full (SGP and MoA) and filtered (GP) database models.

Table 2 Restitution percent absolute error metrics on the drag coefficient.

| | SGP Sq Exp | SGP Exp | MoA Sq Exp | MoA Exp | GP Sq Exp | GP Exp × E-06 |
|---------------------------------|---------------|------------|---------------|------------|--------------|------------------|
| Mean (%) | 1.65 | 2.93 | 1.24 | 2.29 | 0.28 | 1.43 |
| Max (%) | 16.33 | 20.92 | 27.33 | 55.80 | 8.40 | 54.6 |
| Median (%) | 0.72 | 2.07 | 0.32 | 0.21 | 0.15 | 0.46 |
| 95 th Percentile (%) | 6.01 | 8.71 | 5.43 | 12.79 | 0.96 | 5.72 |
| 99 th Percentile (%) | 8.77 | 12.32 | 13.48 | 26.56 | 2.49 | 15.3 |
| RMSE or RRMS (%) | 2.68 | 4.04 | 2.82 | 5.74 | 0.62 | 3.81 |

C. Verification results

The results for the verification step are shown in the box-and-whiskers plot in Figure 8 with the corresponding error metrics in Table 3. The prediction errors of all the candidate models are low on average, although they are significantly lower for the GP models. Moreover, their spread as shown through the associated whiskers is noticeably more limited to lower values for the GP models. The SGP and MoA model predictions at locations unknown to the training set are poorest. The GP models show significantly better predictive abilities, with RRMS values of 1.17 for the squared exponential kernel and 2.18 for the exponential kernel. For the best-performing model (GP with a squared exponential kernel), the verification error, which represents the ability to predict the drag coefficient at a location completely unknown to the surrogate model, is within 2.52% 95% of the time, and within 3.81% of the time, for this verification set.

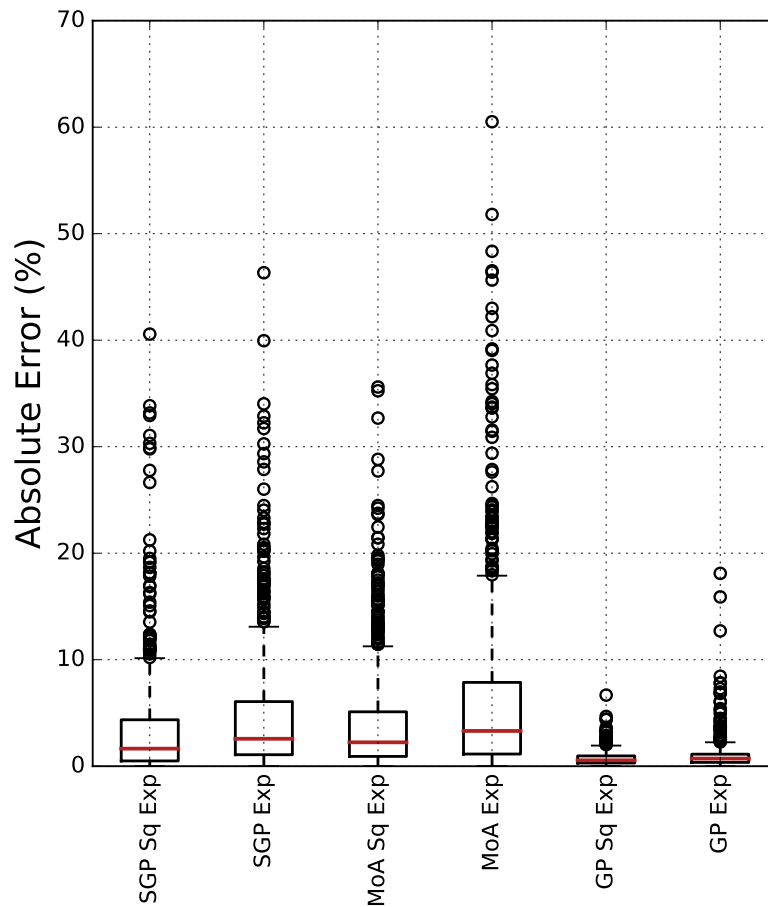


Fig. 8 Verification results for full (SGP and MoA) and filtered (GP) database models.

D. Overall performance

In all three testing steps, the SGP and MoA models perform poorly owing to oversmoothing and overfitting, respectively. The SGP and MoA models considered using the provided dataset cannot adequately replace the underlying

Table 3 Verification percent absolute error metrics on the drag coefficient for full and filtered database models.

| | SGP Sq Exp | SGP Exp | MoA Sq Exp | MoA Exp | GP Sq Exp | GP Exp |
|---------------------------------|---------------|------------|---------------|------------|--------------|-----------|
| Mean (%) | 3.34 | 4.66 | 4.08 | 6.22 | 0.82 | 1.17 |
| Max (%) | 40.57 | 46.33 | 35.60 | 60.51 | 6.68 | 18.11 |
| Median (%) | 1.65 | 2.58 | 2.24 | 3.31 | 0.55 | 0.72 |
| 95 th Percentile (%) | 11.34 | 17.09 | 15.33 | 22.64 | 2.52 | 3.86 |
| 99 th Percentile (%) | 28.22 | 28.75 | 23.65 | 41.19 | 3.81 | 7.99 |
| RMSE or RRMS (%) | 5.89 | 7.43 | 6.50 | 10.32 | 1.17 | 2.18 |

CFD-based aerodynamic optimization process. The more targeted approach of database size reduction to allow for GP model construction provides better results by avoiding both oversmoothing and overfitting.

The particularly poor estimates for the flight conditions corresponding to high angles of attack and high Mach numbers can be explained by the fact that wave drag suddenly becomes a significant part of the total drag in these cases. When shock waves are formed at high flow incidence and/or Mach number, the additional associated drag is poorly taken into account by the surrogate models. Moreover, shock wave formation is highly dependent on the optimized airfoil shapes, since the aerodynamic optimization process only seeks to find $\mathbf{s}^*(\mathbf{x}_p)$ with the lowest total drag, which translates to zero or near-zero wave drag. As a result, there can be no strict expectations as to how coherent the behavior of the wave drag component should be beyond the cruise condition.

Between the two GP models, the one with a squared exponential kernel outperforms its exponential kernel counterpart, with lower mean, maximum and RRMS values of the percent absolute error. The near-zero restitution error of the exponential kernel model indicates that the non-smoothness associated with this covariance function allows the model to pass through all the training points without difficulty. However, the squared exponential kernel model provides noticeably better predictions than the exponential kernel model for the verification set, where an RRMS of 1.17 is measured for the squared exponential kernel compared to 2.18 for the exponential kernel. It is important to note that the verification set is made up of points obtained through an adaptive DoE technique, where additional sampling is suggested in regions where knowledge is poorest to enrich the training database most efficiently. The superior performance of a smooth kernel over a non-smooth kernel also matches expectations because almost all physical processes are continuously differentiable everywhere [47] rather than nowhere.

E. Model selection

Based on the results shown, the GP model with a squared exponential kernel is selected for integration in the mission analysis module of the OAD analysis chain for the BWB. Results from Table 3 in the verification step show that predictions for this dataset were within 2.5% of the true value 95% of the time, and within 3.8% of the true value 99% of the time. Scatter plots showing the similarity between true and predicted values for the validation, restitution, and

verification steps are shown in Figures 9, 10 and 11.

For the cross-validation results, it can be seen that the two highest levels of error occur for the two highest drag coefficient values, which correspond to the most loaded flight conditions, i.e. highest M and α . The same effect is found in the restitution results, where the selected surrogate model matches the supplied data closely, with only some mild deviations occurring for drag coefficients over 200 drag counts. The verification results show that the selected model has satisfactory predictive capabilities, with the predicted values matching the true values within 3 drag counts 95% of the time, and within 0.9 drag count on average. The good verification performance suggests that the points in the domain provided by training set used are well-distributed all over the design space, providing good conditions for interpolation i.e. within the bounds of available knowledge and sufficient availability of neighboring data.

Among the discarded models, the next best ten-fold cross-validation RRMS value is at best 1.56 times higher than that of the selected model, corresponding to the GP with an exponential kernel. Similarly, for restitution RRMS value, the next best RRMS value is 4.32 times higher, excluding the GP model with an exponential which perfectly fits but also overfits the input data. As for the verification RRMS values, the next best model is again the GP with an exponential kernel, with 1.86 times higher RRMS than the selected model.

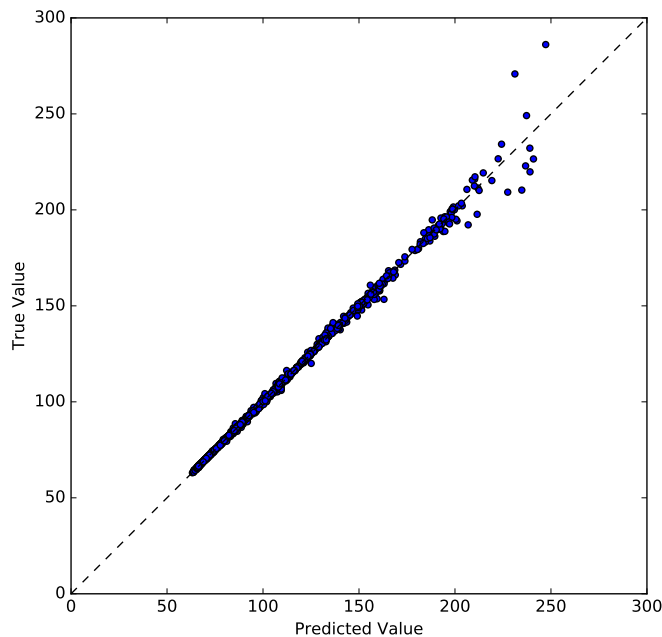


Fig. 9 Ten-fold cross-validation error on the selected surrogate model, in drag counts.

Conclusion

In this paper, the development of a surrogate model based on GPs to replace a complex high-speed aerodynamic optimization and evaluation process for a BWB aircraft is presented. The intended use of this surrogate model is for

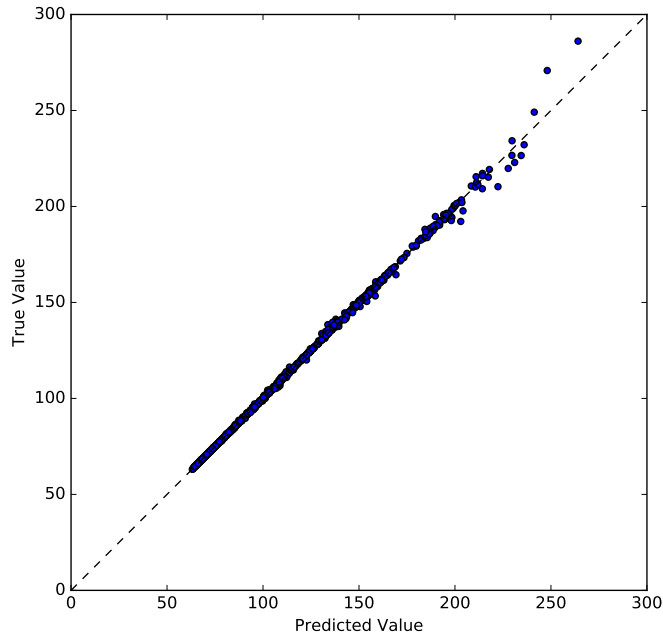


Fig. 10 Restitution error on the selected surrogate model, in drag counts.

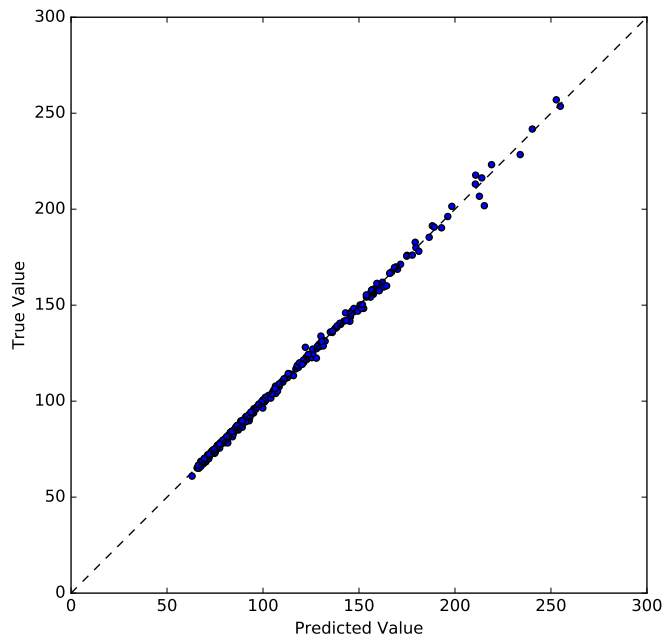


Fig. 11 Verification error on the selected surrogate model, in drag counts.

mission analysis module in multidisciplinary OAD at the conceptual phase. A training set consisting of the drag polars for 48 BWB planform shapes is initially available, containing 2869 data points. Models based on the full database employing the MoA and SGP techniques do not perform well owing to the appearance of transonic effects at high M

and/or α . To alleviate the need to use specialized GP-based techniques and use GPs directly, the size of the training set is reduced to 1355 data points by keeping only the points that show pertinence to the mission analysis process. Of the six models tested, the GP with a squared exponential covariance function showed the best overall performance. For the selected model, the 95th percentile of the prediction error is 1.75% for ten-fold cross-validation, 0.96% for restitution, and 2.52% for verification. The 95th percentile conveniently englobes the C_D values corresponding to the most solicited fundamental range of C_L values in BWB mission analysis of 0.17 to 0.32, such that at most 2.52% prediction error can be assumed on C_D for the fundamental C_L range. Similarly, the 99th percentile of the prediction error is 3.60% for ten-fold validation, 2.49% for restitution, and 3.81% for verification, such that it can be assumed that the prediction error is at most 3.81% beyond the fundamental C_L range, presuming higher error occurrences are attributable to the single-point nature of the aerodynamic optimization process, which does not expressly consider the compressibility drag for high Mach and/or angle of attack flight conditions. As a consequence of single-point optimization, it can be expected that a solution very close to the cruise-optimal one exists that meets the predicted C_D values for high C_L conditions. Finally, in terms of time savings, the selected GP model with a squared exponential kernel for the filtered training set provides the cruise-optimal high-speed aerodynamic performance for any BWB planform shape within the design bounds in under a minute on a personal computer. This is considerably lower than the CFD-based process, which takes 175 hours using 32 processors on an HPC5 supercomputer.

References

- [1] ATAG, "Facts and Figures," <https://www.atag.org/facts-figures.html>, 2020. Accessed: 2020-02-17.
- [2] International Air Transport Association, "Fact sheet: Climate change & CORSIA," *A40-WP/54*, 2019. Retrieved from https://www.iata.org/pressroom/facts_figures/fact_sheets/Documents/fact-sheet-climate-change.pdf.
- [3] Brelje, B. J., and Martins, J. R., "Electric, hybrid, and turboelectric fixed-wing aircraft: A review of concepts, models, and design approaches," *Progress in Aerospace Sciences*, Vol. 104, 2019, pp. 1–19.
- [4] Jansen, R., Bowman, C., Jankovsky, A., Dyson, R., and Felder, J., "Overview of NASA electrified aircraft propulsion (EAP) research for large subsonic transports," *53rd AIAA/SAE/ASEE Joint Propulsion Conference*, 2017, p. 4701.
- [5] Sarlioglu, B., and Morris, C. T., "More electric aircraft: Review, challenges, and opportunities for commercial transport aircraft," *IEEE transactions on Transportation Electrification*, Vol. 1, No. 1, 2015, pp. 54–64.
- [6] Tremolet, A., Gauvrit-Ledogar, J., Brevault, L., Defoort, S., Morel, F., and Gauvrit, J., "Multidisciplinary Overall Aircraft Design and Optimization of Blended Wing Body Configurations," *8th European Conference for Aeronautics and Space Sciences (EUCASS)*, 2019, pp. 1–15. <https://doi.org/10.13009/EUCASS2019-900>.
- [7] Bijewitz, J., Seitz, A., Hornung, M., and Luftfahrt eV, B., "A review of recent aircraft concepts employing synergistic

- propulsion-airframe integration,” *30th Congress of the International Council of the Aeronautical Sciences, Daejeon, Korea*, 2016, pp. 1–21.
- [8] Liou, M.-F., Kim, H., Lee, B., and Liou, M.-S., “Aerodynamic Design of the Hybrid Wing Body Propulsion-Airframe Integration,” *NASA NTRS*, 2017.
- [9] Hendricks, E., and Tong, M., “Performance and weight estimates for an advanced open rotor engine,” *48th AIAA/ASME/SAE/ASEE Joint Propulsion Conference & Exhibit*, 2012, p. 3911.
- [10] Hall, D. K., Huang, A. C., Uranga, A., Greitzer, E. M., Drela, M., and Sato, S., “Boundary layer ingestion propulsion benefit for transport aircraft,” *Journal of Propulsion and Power*, Vol. 33, No. 5, 2017, pp. 1118–1129.
- [11] Arntz, A., and Atinault, O., “Exergy-Based Performance Assessment of a Blended Wing–Body with Boundary-Layer Ingestion,” *AIAA journal*, Vol. 53, No. 12, 2015, pp. 3766–3776.
- [12] Sievers, M., and Wheaton, M., “Blended wing body architecting and design: current status and future prospects,” *Procedia Computer Science*, Vol. 28, 2014, pp. 619–625.
- [13] Martinez-Val, R., Cuerno, C., Perez, E., and Ghigliazza, H. H., “Potential effects of blended wing bodies on the air transportation system,” *Journal of aircraft*, Vol. 47, No. 5, 2010, pp. 1599–1604.
- [14] “X-48 Research: All good things must come to an end | NASA,” https://www.nasa.gov/topics/aeronautics/features/X-48_research_ends.html, 2013. Accessed: 2020-02-17.
- [15] “Airbus reveals its blended wing aircraft demonstrator,” <https://www.airbus.com/newsroom/press-releases/en/2020/02/airbus-reveals-its-blended-wing-aircraft-demonstrator.html>, 2020. Accessed: 2020-02-17.
- [16] Lyu, Z., and Martins, J. R., “Aerodynamic design optimization studies of a blended-wing-body aircraft,” *Journal of Aircraft*, Vol. 51, No. 5, 2014, pp. 1604–1617.
- [17] Denieul, Y., Bordeneuve, J., Alazard, D., Toussaint, C., and Taquin, G., “Multicontrol surface optimization for blended wing–body under handling quality constraints,” *Journal of Aircraft*, Vol. 55, No. 2, 2018, pp. 638–651.
- [18] Feldstein, A., Lazzara, D., Princen, N., and Willcox, K., “Multifidelity data fusion: application to blended-wing-body multidisciplinary analysis under uncertainty,” *AIAA Journal*, Vol. 58, No. 2, 2020, pp. 889–906.
- [19] Li, Y., and Qin, N., “Influence of Spanwise Load Distribution on Blended-Wing–Body Performance at Transonic Speed,” *Journal of Aircraft*, Vol. 57, No. 3, 2020, pp. 408–417.
- [20] Bevan, R., Poole, D., Allen, C., and Rendall, T., “Adaptive surrogate-based optimization of vortex generators for tiltrotor geometry,” *Journal of Aircraft*, Vol. 54, No. 3, 2017, pp. 1011–1024.
- [21] Wauters, J., and Degroote, J., “Surrogate-Assisted Parametric Study of a Wing Fences for Unmanned Aerial Vehicles,” *Journal of Aircraft*, Vol. 58, No. 3, 2021, pp. 562–579.

- [22] Han, Z.-H., Chen, J., Zhang, K.-S., Xu, Z.-M., Zhu, Z., and Song, W.-P., “Aerodynamic shape optimization of natural-laminar-flow wing using surrogate-based approach,” *AIAA Journal*, Vol. 56, No. 7, 2018, pp. 2579–2593.
- [23] Leifsson, L., Koziel, S., and Tesfahunegn, Y. A., “Multiobjective aerodynamic optimization by variable-fidelity models and response surface surrogates,” *AIAA Journal*, Vol. 54, No. 2, 2016, pp. 531–541.
- [24] Li, J., and Cai, J., “Massively multipoint Aerodynamic shape design via surrogate-assisted gradient-based optimization,” *AIAA Journal*, Vol. 58, No. 5, 2020, pp. 1949–1963.
- [25] Zhang, J., and Zhao, X., “Machine-Learning-Based Surrogate Modeling of Aerodynamic Flow Around Distributed Structures,” *AIAA Journal*, Vol. 59, No. 3, 2021, pp. 868–879.
- [26] Clark Jr, D. L., Bae, H., and Forster, E. E., “Gaussian Surrogate Dimension Reduction for Efficient Reliability-Based Design Optimization,” *AIAA Journal*, Vol. 58, No. 11, 2020, pp. 4736–4750.
- [27] Kwon, H., Choi, S., Kwon, J.-H., and Lee, D., “Surrogate-Based Robust Optimization and Design to Unsteady Low-Noise Open Rotors,” *Journal of Aircraft*, Vol. 53, No. 5, 2016, pp. 1448–1467.
- [28] Mialon, B., Fol, T., and Bonnaud, C., “Aerodynamic optimization of subsonic flying wing configurations,” *20th AIAA applied aerodynamics conference*, 2002, p. 2931.
- [29] Roman, D., Gilmore, R., and Wakayama, S., “Aerodynamics of high-subsonic blended-wing-body configurations,” *41st Aerospace Sciences Meeting and Exhibit*, 2003, p. 554.
- [30] Gebbie, D. A., Reeder, M. F., Tyler, C., Fonov, V., and Crafton, J., “Lift and drag characteristics of a blended-wing body aircraft,” *Journal of aircraft*, Vol. 44, No. 5, 2007, pp. 1409–1421.
- [31] Sripawadkul, V., Padulo, M., and Guenov, M., “A comparison of airfoil shape parameterization techniques for early design optimization,” *13th AIAA/ISSMO multidisciplinary analysis optimization conference*, 2010, p. 9050.
- [32] Piegl, L., and Tiller, W., *The NURBS book*, Springer Science & Business Media, 2012.
- [33] Aubeelack, H., Segonds, S., Bes, C., Druot, T., Bérard, A., Duffau, M., and Gallant, G., “A new robust optimal design methodology with acceptable risks: An application to BWB aircraft,” *AIAA Journal*, in press.
- [34] Cambier, L., Heib, S., and Plot, S., “The Onera elsA CFD software: input from research and feedback from industry,” *Mechanics & Industry*, Vol. 14, No. 3, 2013, pp. 159–174.
- [35] Spalart, P., and Allmaras, S., “A one-equation turbulence model for aerodynamic flows,” *30th aerospace sciences meeting and exhibit*, 1992, p. 439.
- [36] Hirsch, C., *Numerical computation of internal and external flows: The fundamentals of computational fluid dynamics*, Elsevier, 2007.

- [37] Hue, D., and Esquieu, S., “Computational drag prediction of the DPW4 configuration using the far-field approach,” *Journal of aircraft*, Vol. 48, No. 5, 2011, pp. 1658–1670.
- [38] Belyaev, M., Burnaev, E., Kapushev, E., Panov, M., Prikhodko, P., Vetrov, D., and Yarotsky, D., “Gtapprox: Surrogate modeling for industrial design,” *Advances in Engineering Software*, Vol. 102, 2016, pp. 29–39.
- [39] Rasmussen, C. E., “Gaussian processes in machine learning,” *Summer School on Machine Learning*, Springer, 2003, pp. 63–71.
- [40] Duvenaud, D. K., Nickisch, H., and Rasmussen, C. E., “Additive gaussian processes,” *Advances in neural information processing systems*, 2011, pp. 226–234.
- [41] Wang, W., and Haaland, B., “Controlling Sources of Inaccuracy in Stochastic Kriging,” *Technometrics*, Vol. 61, No. 3, 2019, pp. 309–321. <https://doi.org/10.1080/00401706.2018.1514328>, URL <https://doi.org/10.1080/00401706.2018.1514328>.
- [42] Foster, L., Waagen, A., Aijaz, N., Hurley, M., Luis, A., Rinsky, J., Satyavolu, C., Way, M. J., Gazis, P., and Srivastava, A., “Stable and Efficient Gaussian Process Calculations.” *Journal of Machine Learning Research*, Vol. 10, No. 4, 2009.
- [43] Williams, C. K., and Seeger, M., “Using the Nyström method to speed up kernel machines,” *Advances in neural information processing systems*, 2001, pp. 682–688.
- [44] Hastie, T., Tibshirani, R., and Friedman, J., *The elements of statistical learning: data mining, inference, and prediction*, Springer Science & Business Media, 2009.
- [45] Schwarz, G., et al., “Estimating the dimension of a model,” *The annals of statistics*, Vol. 6, No. 2, 1978, pp. 461–464.
- [46] Queipo, N. V., Haftka, R. T., Shyy, W., Goel, T., Vaidyanathan, R., and Tucker, P. K., “Surrogate-based analysis and optimization,” *Progress in aerospace sciences*, Vol. 41, No. 1, 2005, pp. 1–28.
- [47] Galperin, E., “Some old traditions in mathematics and in mathematical education,” *Computers & Mathematics with Applications*, Vol. 37, No. 4-5, 1999, pp. 9–17.